J Mater Sci (2010) 45:4745–4753
DOI 10.1007/s10853-010-4426-3

ULTRAFINE GRAINED MATERIALS

Ultrahigh strength of nanocrystalline iron-based alloys produced by high-pressure torsion

Tadahiko Furuta · Shigeru Kuramoto · Kayo Horibuchi · Tetsu Ohsuna · Zenji Horita

Received: 9 February 2010 / Accepted: 17 March 2010 / Published online: 8 April 2010

Abstract Microstructural evolution of an Fe–18.1% Ni–34.9%Co–9.3%Ti (in at.%) in processing by high-pressure torsion (HPT) was investigated by electron backscatter diffraction. After 10 turns of HPT straining at room temperature with a rotation speed of 1 rpm under a pressure of 6 GPa, the alloy was composed of body-centered cubic-structured grains with sizes of 20–50 nm having high density crystal defects inside the grains. The mechanism of this significant grain refinement was discussed in relation to the stress-induced martensitic transformation and transgranular shear near ideal strength. The actual shear stress of the nanocrystalline iron-based alloy was estimated to be 1.37 GPa and as high as 38% of the ideal shear stress, which is similar to Gum Metal exhibiting deformation without dislocation activity. It is inferred from these results that the dislocation motion can be suppressed up to ultra-high stress level near ideal strength by the formation of nano-sized grains.

Introduction

Grain refinement of metallic materials is an effective approach to achieve an ultra-high strength. There have been a number of attempts to produce nanostructured materials using severe plastic deformation (SPD) [1] such as equal-channel angular pressing (ECAP) [2], accumulative roll bonding (ARB) [3], and high-pressure torsion (HPT) [4]. It is well known that these processes promote greater hardening through the significant grain refinement with high density crystal defects.

Recently, we have found an iron-based alloy, Fe–18.1%Ni–34.9%Co–9.3%Ti (in at.%) [5], which is composed of nano-grains having sizes of 20–50 nm with body-centered cubic (bcc) crystal structure after processing by HPT under a pressure of 6 GPa for 10 turns. The ultimate tensile strength (UTS) of this HPT-processed iron-based alloy is 2.73 GPa, which results in the strength being twice as much as the UTS prior to the HPT process. Thus, when the UTS is normalized by the Young's modulus (E), 144 GPa, the normalized ratio reaches $\sim$0.018 and this is considerably higher than the ratio of at most $\sim$0.011 obtained in the conventional crystalline alloys. The lower UTS/E value for the latter in the conventional alloys can be explained by dislocation theory [6–8], which describes the deformation occurring through the movement of dislocations before the applied stress increases up to the ideal shear stress. In addition, it is noted that the HPT-processed iron-based alloy still has a total elongation to failure of 8–10%. Simultaneous achievement of the ultra-high strength and the high ductility is extremely difficult in conventional metallic materials. This is because dislocations governing the plastic deformation are heavily pinned by some obstacles in the high strength alloys. Regarding the trade-off relation between the strength and the ductility, the grain refinement by SPD has been reported to improve both of them simultaneously [1, 9]. In such reports, the improved elongation of more than 30% has been achieved; however, the reported values of 0.003–0.007 for UTS/E are

T. Furuta (✉) · S. Kuramoto
Frontier Research Center, Toyota Central R&D Laboratories Inc., Nagakute, Aichi 480-1192, Japan
e-mail: e0646@mosk.tytlabs.co.jp

K. Horibuchi · T. Ohsuna
Materials-Analysis Lab., Toyota Central R&D Laboratories Inc., Nagakute, Aichi 480-1192, Japan

Z. Horita
Department of Materials Science and Engineering, Faculty of Engineering, Kyushu University, Fukuoka 819-0395, Japan

substantially smaller than that of the HPT-processed iron-based alloy.

In the present study, microstructural evolution during HPT process was investigated by electron backscatter diffraction (EBSD) analysis using the Fe–18.1%Ni–34.9%Co–9.3%Ti alloy. The grain refinement process will be discussed in relation to deformation-induced phase transformation. Furthermore, a possible mechanism for the high UTS/*E* value of the alloy will be discussed in comparison with Gum Metal [10] in which plastic deformation is likely to proceed near ideal strength without dislocation motion.

Experimental procedures

An Fe–18.1%Ni–34.9%Co–9.3%Ti alloy was melted using high purity raw metals and cast in an iron mold under argon atmosphere. The ingot was hot-forged at 1,423 K into a round bar with 15 mm diameter. The bar was then solution treated at 1,373 K for 86.4 ks in an argon atmosphere, and quenched in water. Disc specimens of 10 mm diameter and 0.8 mm height, *h*, for HPT were prepared from the solution-treated bar (Fig. 1a, b). A disc specimen was placed between upper and lower anvils and torsion-strained by rotating the lower anvil at a rotation speed of 1 rpm under a compression stress of 6 GPa, for a selected number of turns, *N*, equal to 0.5, 1, 5, and 10 at room temperature. Here, the equivalent strain, ε, was calculated using the following relation:

$$\varepsilon = 2\pi Nr/h3^{1/2}, \quad (1)$$

where *r* is the distance from the disc center [11].

Hardness was measured by a Vickers microhardness tester at a load of 100 g for 30 s. The hardness measurements were performed on the cross-sectional plane as illustrated in Fig. 1b. Microstructural characterization was conducted using scanning electron microscopy (SEM) and EBSD. The areas for EBSD measurement were selected from the region of 0.4 mm height at the radial cross-section plane for $N = 0.5$ and 1. Measurement step in EBSD was 0.02 or 1.5 μm, and only the data points with Image Quality and Confidence Index over 60 and 80, respectively, were used for further analysis to exclude the unreliable data points. The areas for SEM observation and EBSD evaluation are also indicated in Fig. 1c.

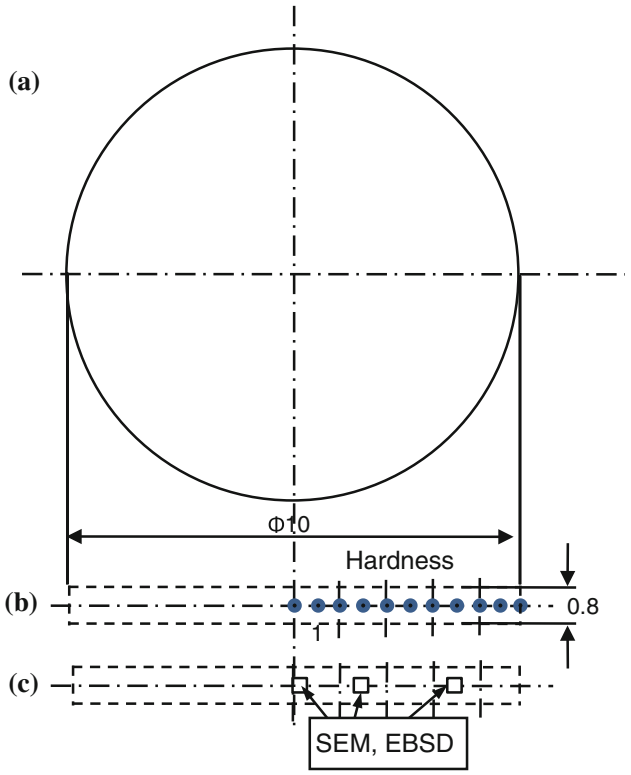

Fig. 1 Specimen for HPT straining and positions for evaluations on cross section. **a** Whole specimen, **b** points of hardness measurements, **c** areas for SEM, EBSD observations

Results and discussion

Beginning of grain refinement in the very early stage of HPT straining

Figure 2 shows changes in hardness with distance from the disc center. The hardness of the solution-treated specimen is ~3.5 GPa and this is indicated by the horizontal dotted line. The hardness in the specimen for $N = 1$ gradually increases with distance from the center and appears to

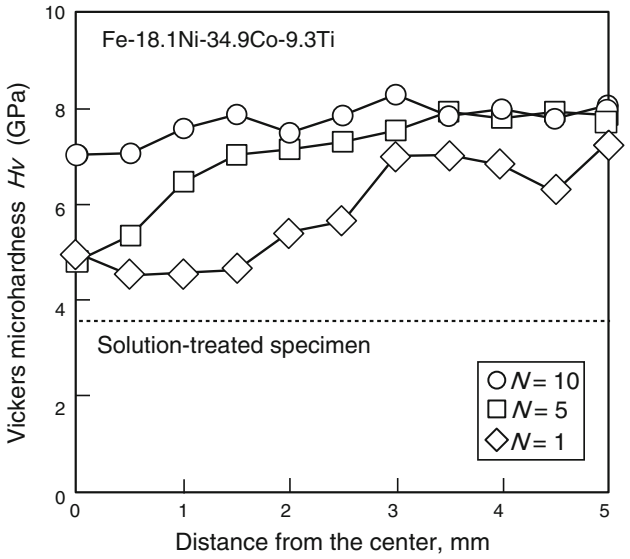

Fig. 2 Radial distributions of Vickers microhardness in Fe–18.1%Ni–34.9%Co–9.3%Ti discs produced by HPT at rotation speed of 1 rpm for *N* turns at room temperature

saturate at 3.5 mm to a hardness of 6–7 GPa. This variation of hardness from the center to the edge region may be due to inhomogeneous development of the microstructure at an early stage of torsion straining. In the specimen of $N = 5$, tendency of hardness distribution is similar to the specimen of $N = 1$, but the distance for the saturation becomes shorter and the hardness level for the saturation increase to about 8 GPa. The hardness in the specimen of $N = 10$ remains approximately constant from the center to edge in the specimen. The hardness values at the center in these HPT-processed specimens are higher than that after the solution treatment despite the fact that the equivalent strain is theoretically zero at the center in HPT. This may be attributed to the increased density of geometrically necessary dislocations during HPT [12] or inaccurate sampling position in the present hardness measurements.

All the hardness values in Fig. 2 are re-plotted as a function of equivalent strain in Fig. 3. From the X-ray diffraction analysis in the previous study [13], the phase of the alloy changes during HPT so that such changes are also indicated in the figure. The solution-treated specimen consists of a γ phase with face-centered cubic (fcc) crystal structure. After processing for one turn ($\varepsilon < 22.6$), the γ phase almost transforms into an α phase with bcc structure by deformation-induced martensitic transformation with a little fraction of the untransformed γ phase remaining in the disc. For five revolutions ($\varepsilon < 113$), the initial γ phase totally transforms into the α phase. It is clear from these results that the hardness increases up to $\sim$7 GPa in the early stage of straining ($\varepsilon = 20$–30) with the γ to α phase transformation, and subsequently reaches a steady state

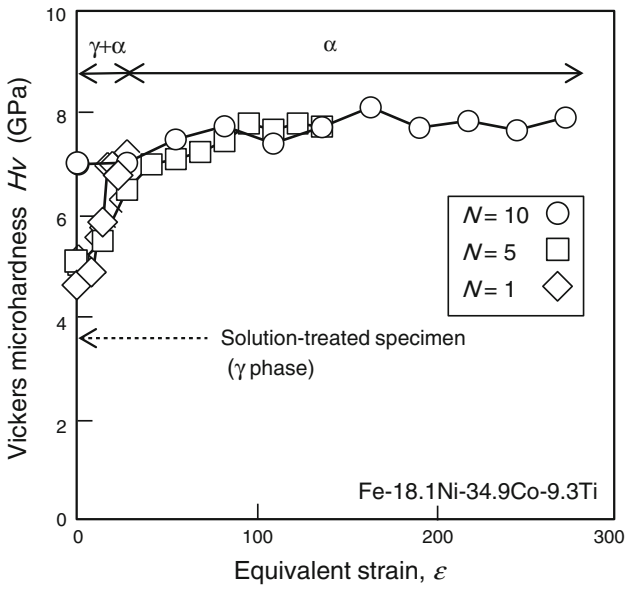

Fig. 3 Vickers microhardness as function of equivalent strain after HPT along with observed phases by XRD

where the hardness remains almost unchanged in the α phase with further straining. Therefore, it is important to investigate changes in microstructure in the early stage of straining in order to understand the strengthening behavior of the present iron-based alloy.

Figure 4 shows SEM images at 0.2 and 1.5 mm from the center of the specimen for $N = 0.5$, where ε is 0.45 and 3.4, respectively, along with inverse pole figure (IPF) maps for both γ and α phases obtained from the EBSD analysis. In Fig. 4a, b, c at $\varepsilon = 0.45$, the microstructure consists of slightly elongated γ grains with the average grain size of 100–200 μm, being not much different in grain size from the initial state of the solution-treated specimen. In Fig. 4d, e, f at $\varepsilon = 3.4$, a lamellar microstructure appears by further HPT straining. It is clear from the results of crystal orientation analysis of EBSD in Fig. 4e, f that the lamellar-shaped α phase was generated in the γ grains by stress-induced martensitic transformation during HPT. Figure 5 shows the results of detailed analysis on orientation relationship between the initial γ and the induced α. Here, Fig. 5a–d represent an Image Quality map, γ and α phase map, and pole figures (c) for $(111)_\gamma$ and (d) for $(110)_\alpha$, respectively. It is apparent from the pole figures that ND of the induced α phase is almost aligned to (110). Although there is some amount of misorientation, the orientation relationship between the γ and α phases is almost $(111)_\gamma$// $(110)\alpha$. Further orientation analysis on several observed areas exhibited that the habit plane of the transformation is close to $(111)_\gamma$, and that the orientation between the γ and the α is Kurdjumov–Sachs (K–S) relationship, $(111)_\gamma$// $(011)_\alpha$, $\langle 0{-}11\rangle_\gamma // \langle 1{-}11\rangle_\alpha$.

As indicated in Figs. 4 and 5, the lamellar-shaped α phase extends through the whole γ grain with the sizes of 100–200 μm, and the crystal orientation in the induced α phase appears to be aligned in the specific direction from the IPF map (Fig. 4f). Such phase transformation does not seem to be effective in reducing the grain size. However, the pole figure (Fig. 5d) shows that there is some amount of misorientation in the α phase, and variants of α phase from two different habit planes appear in the IPF map (Fig. 4f). Hence, further analysis was made on the induced α phase to determine the detailed orientation distribution after the phase transformation.

Figure 6 shows (a) a detailed orientation map and (b) a corresponding pole figure of an induced α phase where related misorientation profiles and a schematic are also shown. Here, small amount of orientation variation, about 10 degrees, is indicated by color gradation. The orientation in the α phase in Fig. 6a changes gradually from the lower right to the upper left direction. Figure 6c shows misorientation profiles along the arrow shown in Fig. 6a. The misorientation profiles indicate that the misorientation angle between the lower right region and the upper left is

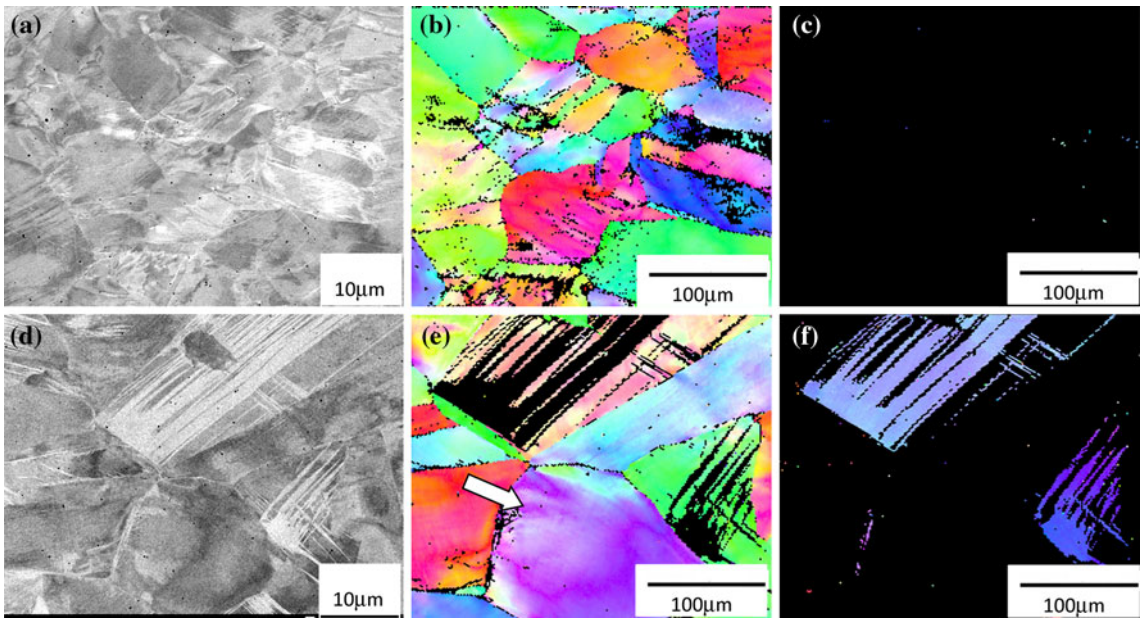

Fig. 4 Microstructure of Fe–18.1%Ni–34.9%Co–9.3%Ti after HPT for $N = 0.5$. **a**, **d** SEM images, **b**, **e** IPF maps for γ phase, and **c**, **d** IPF maps for α phase. (**a**, **b**, **c**) at region of 0.2 mm and (**d**, **e**, **f**) of 1.5 mm from center

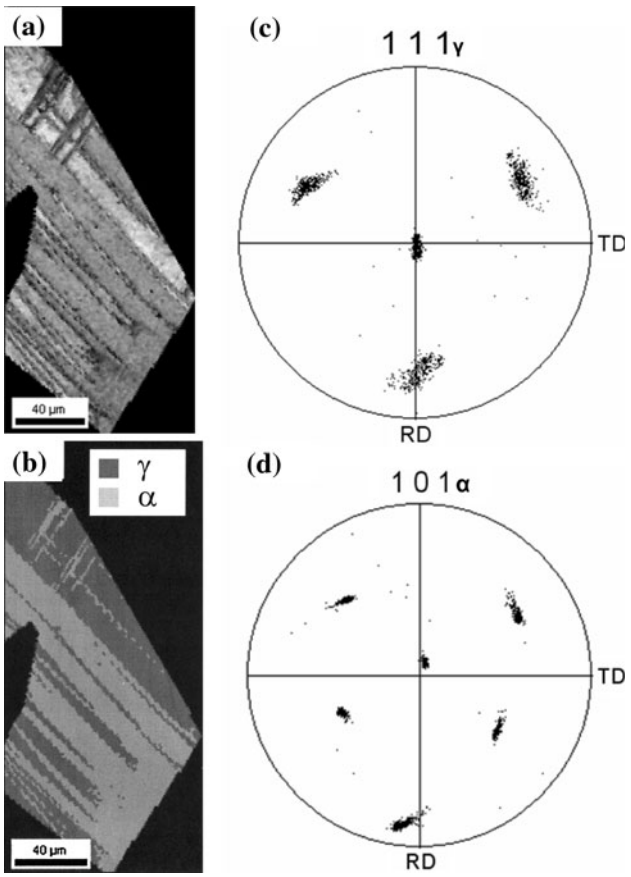

Fig. 5 Orientation analysis on relationship between initial γ and stress-induced α of Fe–18.1%Ni–34.9%Co–9.3%Ti in region 0.2 mm from center after HPT for $N = 0.5$. **a** Image Quality map, **b** γ and α phase map, and pole figures **c** for $(111)_\gamma$ and **d** for $(110)_\alpha$

about 10°, and the orientation gradually changes between the two regions. This misorientation can be seen on the pole figure in Fig. 6b, and is understood by considering two different habit planes for the transformation. In cubic crystals, the angles between neighboring {111} and {110} are 70.5° and 60°, respectively. So, if two different variants are transformed from the same initial γ grain, the resultant misorientation between the two variants would be 10.5° since they have the K–S relationship (Fig. 6d). This misorientation of $\sim 10°$ well coincides with the misorientation observed from EBSD analysis (Fig. 6c) and it can be concluded that stress-induced phase transformation from the γ to the α generates a specific amount of crystal rotation inside the grain due to transformation from different habit planes. It has been reported that there are 24 variants in the K–S relationship, and six variants are expected to be generated from one parent γ grain [14]. The misorientation angles between the six variants are 10.5°, 49.5°, or 60°. Only the variants of the misorientation of 10.5° were observed in the present study, however, there possibly exist the variants with the other misorientation angles. Meanwhile, similar crystal rotation was found in the γ phases (shown by an arrow in Fig. 4e), which have not transformed yet. This phenomenon prominently appears in the retained γ phase at 0.2 mm from the center after $N = 1$, at $\varepsilon = 0.9$. Figure 7 shows (a) an IPF map from such area and (b) misorientation profiles of point-to-origin and point-to-point along the arrow in the IPF map. The transgranular macroscopic crystal rotation of about 50° is developed in the elongated grain without any orientation boundaries.

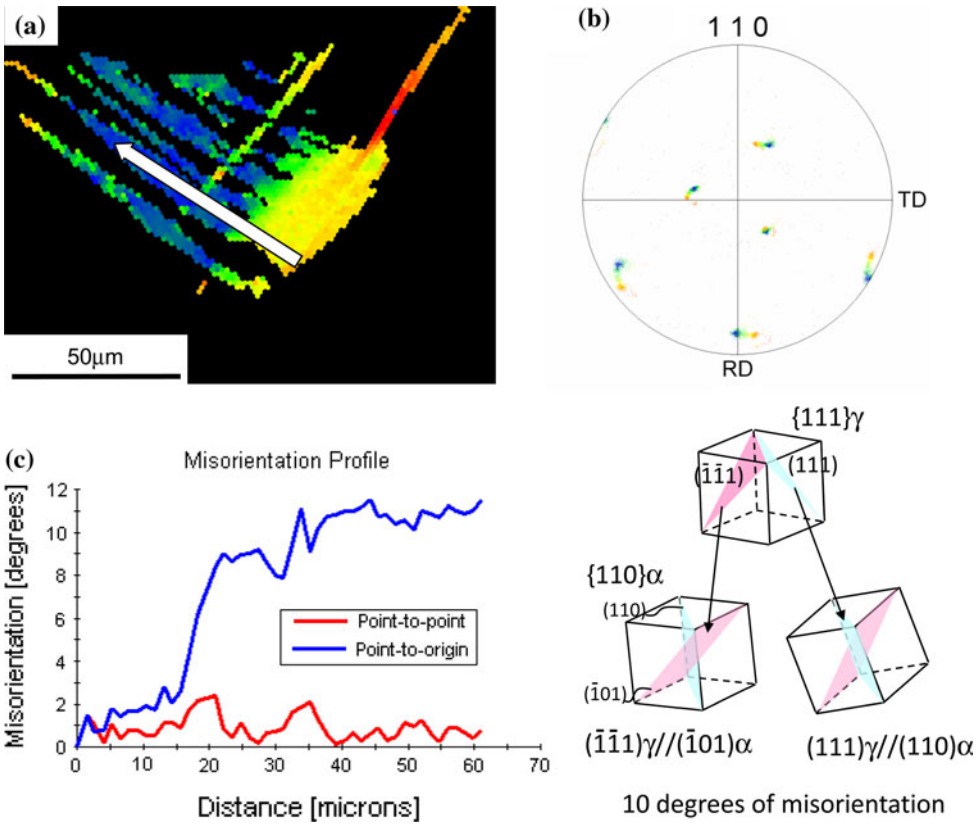

Fig. 6 Detailed orientation map and corresponding pole figure of stress-induced α phase of Fe–18.1%Ni–34.9%Co–9.3%Ti in region 0.2 mm from center after HPT for $N = 0.5$. **a** Orientation map for α phase and **b** pole figure for $\{110\}_\alpha$, **c** misorientation along arrow in (**a**), and **d** schematic of orientation relationships between $\{111\}_\gamma$ and $\{110\}_\alpha$

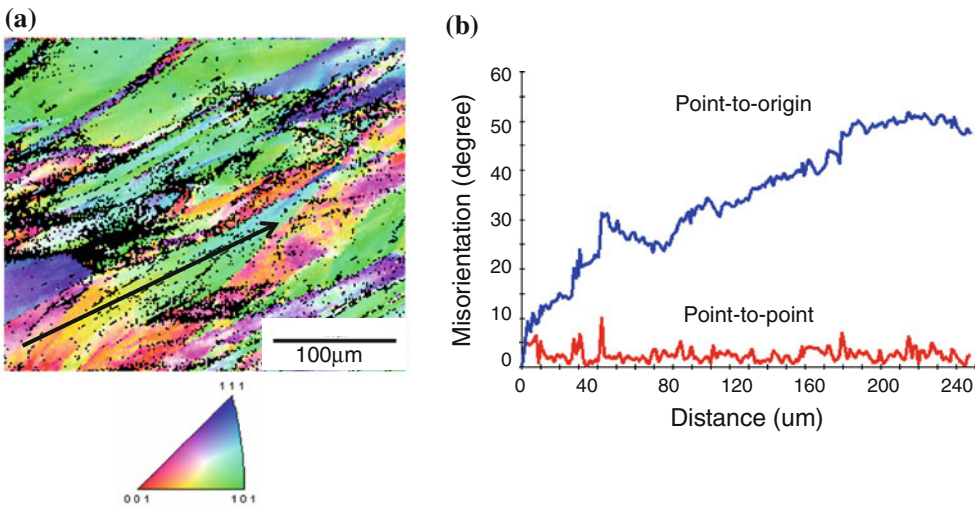

Fig. 7 Misorientation diagram of Fe–18.1%Ni–34.9%Co–9.3%Ti in region of 0.2 mm from center after HPT for $N = 1$. **a** IPF map for γ phase and **b** misorientations along arrow in (**a**)

The initial hardness and the final saturated hardness value are 3.5 and 8 GPa, respectively. The results shown above (Figs. 4, 5, 6, 7) were obtained from where Vickers hardness is 4.5 GPa or lower. This means the changes in microstructure occur in the very early stage of hardening. Based on the EBSD observations shown in Figs. 4, 5, 6, 7 along with the hardness and the phase changes given in Figs. 2 and 3, the beginning of grain refinement may be deduced as follows. In the very early deformation stage until $\varepsilon = 5$, there are two kinds of grain refinement processes from initial γ grain with the sizes of 200–300 μm. One case of the grain refinement is based on the crystal lattice rotation generated by the deformation-induced martensitic transformation from γ to α. Although the rotation angle of about 10° is not enough to make high angle grain boundaries, such low angle orientation gaps would evolve into grain boundaries with higher misorientation angles through subsequent HPT straining. In addition, rearrangements of the variants in the α phase also possibly make new boundaries with 49.5 of 60° [14] during

the subsequent HPT straining. The other case is the grain refinement caused by significant lattice rotation in the initial γ phase shown in Fig. 7. This observation suggests that the α phase is refined after stress-induced transformation, since several number of α variants would be generated upon the transformation from the γ phase with such large orientation variation.

Subsequent grain refinement by further HPT straining

Figure 8 shows (a) SEM images and (b, c) IPF maps at 3.5 mm from the center after $N = 1$ at $\varepsilon = 15.4$. The Vickers hardness was 7 GPa, which is very close to the saturated value of 8 GPa. The grain shape cannot be resolved in the SEM image (Fig. 8a), and there are many black sampling points in the IPF maps (Fig. 8b, c) where the crystal structure and orientation information cannot be acquired because both Image Quality and Confidence Index of obtained EBSD patterns are too low. Only some parts of this area can be indexed and they indicate that there are very fine grains with bcc structure having nearly the same crystal orientation. Here, the grain size of the α phase is less than 500 nm at least and it would be difficult to resolve the size of such small grains by the EBSD method adopted in the present study. Further EBSD analysis was made for several sampling points with more amount of equivalent strain, but no orientation data could be obtained. In the previous studies [5, 13], TEM observation was conducted to measure the grain size at 2.5 mm from the center after $N = 10$, which corresponds to $\varepsilon = 113$. The diffraction pattern exhibited a complete ring, indicating that the microstructure consists of very fine grains having high angle misorientaions. The average grain

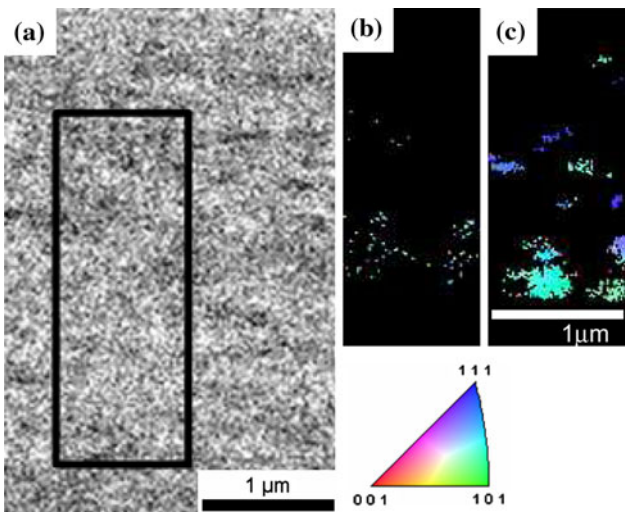

Fig. 8 Microstructure of Fe–18.1%Ni–34.9%Co–9.3%Ti in region 3.5 mm from center after HPT for $N = 1$. **a** SEM micrograph, **b** IPF map for γ phase, and **c** IPF map for α phase

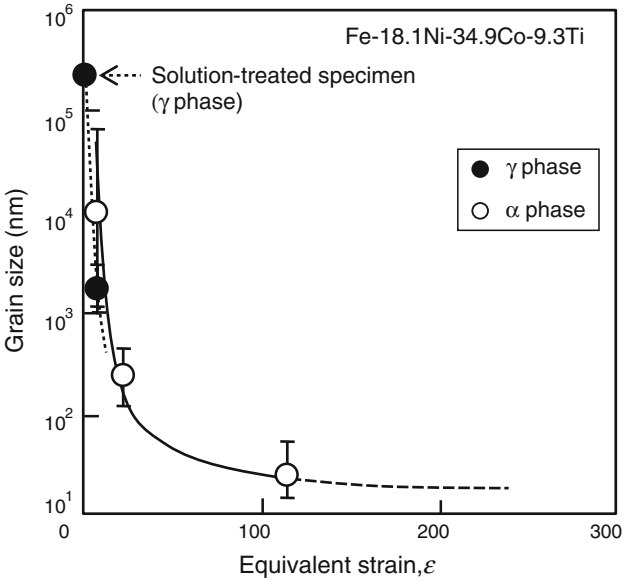

Fig. 9 Grain size in γ and α phase as function of equivalent strain after HPT

sizes of 20–50 nm were observed with high density of crystal defects inside the grain, in which the hardness corresponds to the one at the steady state with ~8 GPa as shown in Fig. 3. There have been a number of reports on grain refinement in the other bcc iron-based alloys by SPD [15], but the reported grain sizes are one order of magnitude larger than the one in the present iron-based alloy. Hence, it is important to understand how the grain refinement proceeds during HPT process in the present iron based alloy in relation to the change in its strength.

Figure 9 shows the grain size in the γ and α phase as a function of the equivalent strain. The grain size was determined from the EBSD results and the plot for $\varepsilon = 113$ was obtained from the previous TEM results [5, 13]. The initial grain size of the γ phase, ~200–300 μm, decreases with increasing equivalent strain, and it reaches the size of 500 nm at $\varepsilon =$ ~3.4. The initial γ phase completely transformed to the α phase up to $\varepsilon = 15.4$ and it was not observed for further straining. The α phase was found at $\varepsilon = 3.4$ and increases the fraction with increasing equivalent strain until it reaches the size of 20–50 nm at $\varepsilon = 113$. Comparing this figure with Fig. 3, the refinement process can be divided into two steps: the first one for the early stage with significant hardening from $\varepsilon = 0$ to $\varepsilon = 20$ and the second one for the later stage with moderate hardening from $\varepsilon = 20$ to $\varepsilon = 100$. To understand the significant grain refinement in the present iron alloy, the refinement process in the later stage with moderate hardening must be studied in detail. Since TEM observations have not been made for specimens in the later stage, the grain refinement process to nanostructure of the present iron based alloy can not be

determined yet. However, we consider that there are two possible mechanisms for the grain refinement.

One mechanism is due to rearrangement of α variants discussed in the previous section. It can be possible that orientation change accompanied by the rearrangement contributes to the grain refinement with increasing misorientation angle at grain boundaries. Such structural transformation [16] or deformation twinning [17] during SPD process has an effect on significant grain refinement; these types of grain refinement are accompanied by cooperative movement of a group of atoms, which is different from gradual structural changes in local area by dislocation motion [16]. The other mechanism is based on grain dividing process by transgranular shear reported in Gum Metal [18], in which dislocation-free plastic deformation mechanism operates near ideal strength. The plastic deformation mechanism in Gum Metal is considered to be related to its unstable crystal structure where $(C_{11}–C_{12})$ takes a very low value. The present iron-based alloy also has the lattice softening along specific orientation similar to the one in Gum Metal [10]. It is well anticipated that the present iron-based alloy has an unstable crystal structure with lattice softening, and grain refinement process similar to Gum Metal operates. The significant refinement of grain size below 100 nm has been reported in the other iron-based bulk alloys, which showed special reverse transformation during HPT process [19, 20]. These reports have shown that the reverse transformation during HPT is essential to the refinement, however, no such reverse transformation was observed in the present study. Since the normal martensitic transformation from γ to α can only exert grain refinement to 100–200 nm [20], we consider that the rearrangement of α variants cannot explain the significant refinement down to 20–50 nm in the present iron based alloy. Additional discussion will be made in the next section in relation to the deformation mechanism.

Strengthening during HPT and deformation mechanism

The Vickers hardness and the yield strength of the present iron-based alloy increase from 3.5 to 8 GPa and from 1.0 to 2.5 GPa [13], respectively, by HPT for $N = 10$. It is well known that Hall–Petch relation, which correlates the grain size with the mechanical properties, is established with the grain size in the range of more than ~100 nm in bulk iron-base alloys, but it has never been reported in the region less than ~100 nm in the bulk iron alloys. There have been reports on the mechanically milled powders with the grain sizes less than 100 nm, and their strength showed lower values than expected from the Hall–Petch relation in the range larger than ~100 nm [21]. In the previous studies [5, 13], the ultrahigh strength of the present iron-based alloy after HPT was attributed to the reduced grain size of 20–50 nm, since the strength of the present iron-based alloy showed similar one in the mechanically milled iron powders with grain sizes of 20–50 nm. The volume fraction of grain boundaries increased to a few tens percent to total volume in such nanocrystalline alloys, so that the dislocation motion can be suppressed up to ultrahigh stress level. The present results show that strengthening mechanism changes from the early stage of HPT straining to the later stage. The orientation map in Fig. 6a with continuous crystal rotation between two α variants indicates that numbers of dislocations were introduced by the γ to α transformation. Thus, the dislocation hardening may be responsible for the work hardening behavior in the early stage. This dislocation hardening in the early stage and subsequent grain refinement together with well-developed high angle grain boundaries after the severe HPT straining of $\varepsilon = 113$, at 2.5 mm from the center after $N = 10$ [13], implies that some kind of dynamic recovery process operated in the later stage of HPT straining, since the amount of hardening became little significant in the later stage. However, the results obtained in the present study are insufficient to explain the whole strengthening mechanism during the HPT process.

The present iron-based alloy has a good ductility with ultrahigh strength as described above, and then let us consider the ideal shear strength, τ_{Ideal}, which is the theoretical shear strength for perfect bcc crystals [22] in order to discuss the possible deformation mechanism of the present iron-based alloy. Here, τ_{Ideal} can be roughly estimated to be 3.2 GPa by using elastic constants of an Fe–36.5 at.%Ni binary alloy [23] with similar lattice softening to the present iron-based alloy. The actual shear stress, τ_{Actual}, in the present iron-based alloy can be estimated as 1.37 GPa [13], and the ratio of the τ_{Actual} to τ_{Ideal} is 38%. Figure 10 compares τ_{Ideal}, τ_{Actual}, and the ratio of $\tau_{Actual}/\tau_{Ideal}$ for several bcc metals including Gum Metal [24], which is known as an engineering ideal strength metallic material. The ratio for

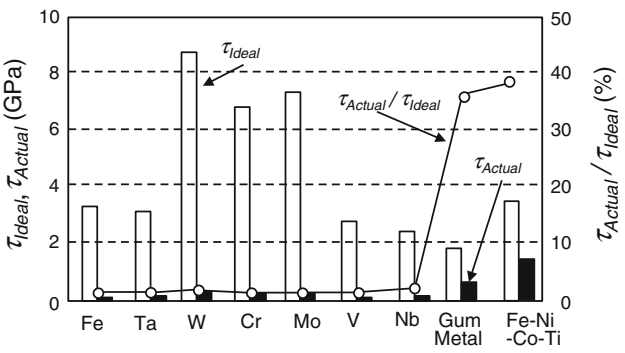

Fig. 10 Comparison of ideal shear stress τ_{Ideal}, actual shear stress τ_{Actual}, and ratio of τ_{Actual} to τ_{Ideal} for several bcc metals including Gum Metal and Fe–18.1%Ni–34.9%Co–9.3%Ti alloy after HPT for $N = 10$

Gum Metal is 36% and this is almost the same as that of the present iron-based alloy. Although the macroscopic stress applied during plastic deformation is lower than the ideal strength in Gum Metal, it is considered that the significant stress concentrations increase local applied stress and enables the deformation near ideal strength [25]. In addition, the in situ nano-pillar compression tests of Gum Metal have shown that the actual deformation strength reaches the ideal one in nano pillars, which deforms uniformly without any significant stress concentrations [26]. In the case of ordinary metals and alloys, the τ_{Actual} is generally decreased to 1/30–1/20 of the τ_{Ideal} but the ratio of $\tau_{Actual}/\tau_{Ideal}$ for the present iron-based alloy and Gum Metal is much higher than the ordinary metals. Although more precise estimation of the ideal strength will be required to discuss the detailed deformation mechanism, the rough estimation here implies that the strength of the present iron-based alloy produced by HPT is approaching ideal shear strength. Such mechanism free from dislocation activity at ideal strength may be related to the improved ductility of the present iron-based alloy, and would also explain the mechanism for the significant grain refinement. In the lattice softened alloys like Gum Metal and the present iron-based alloy, localized elastic softening occurs along $\langle 111 \rangle$ direction, which is the easy glide direction in bcc crystals. When the local stress is increased nearly equal to the ideal shear strength with the aid of some stress concentrations, a transgranular shear could proceed spontaneously across the maximum shear stress plane. Such transgranular shear can contribute to the grain division in α grains in the present case. The hardness of the specimen at equivalent strain of 15.4 was 7 GPa (Figs. 2, 3), which is 88% of the saturated hardness value of 8 GPa. Thus, the applied stress is considered to be high enough to exert the deformation mechanism without dislocation activity in the later stage of HPT straining. The deformation mechanism of the present iron-based alloy along with the grain refinement mechanism will have to be investigated further by critical characterization of microstructure during HPT process.

Conclusions

1. The initial microstructure of solution-treated Fe–18.1%Ni–34.9%Co–9.3%Ti alloy consisted of coarse γ grains, in which lamellar-shaped α phase was induced by martensitic transformation in the early stage of HPT straining. Subsequent straining in the later stage of HPT generated very fine α grains with the size of 20 to 50 nm. The mechanism of this significant grain refinement throughout the specimen was discussed in relation to martensitic transformation and transgranular shear near ideal strength.
2. The hardness of the Fe–18.1%Ni–34.9%Co–9.3%Ti alloy increased from 3.5 to 7 GPa in the early stage of straining by HPT, and subsequently increased up to 8 GPa in the later stage of straining. The significant hardening in the early stage was considered to be related to the increase in dislocation density accompanied by the γ to α transformation. The moderate hardening in the later stage implies refinement of grains with some dynamic structural recovery.
3. The actual shear stress in the HPT-processed Fe–18.1%Ni–34.9%Co–9.3%Ti alloy would be estimated about 1.37 GPa and as high as 38% of the ideal shear stress, similar to Gum Metal, which is considered to deform without dislocation activity. Such a deformation mechanism can explain the ultrahigh strength along with good ductility as well as the significant grain refinement in the present iron-based alloy.

Acknowledgement The authors gratefully acknowledge the assistance of Akira Yamada and Nobuaki Suzuki at Toyota Central R&D Labs., Inc.

References

1. Valiev RZ (2004) Nature Mater 3:511
2. Segal VM, Reznikov VI, Drobyshevskiy AE, Kopylov VI (1981) Russ Metall 1:99
3. Saito Y, Tsuji N, Utsunomiya H, Sakaki T, Hong RG (1998) Scr Mater 39:1221
4. Bridgman PW (1935) Phys Rev 48:825
5. Kuramoto S, Furuta T, Nagasako N, Horita Z (2009) Appl Phys Lett 211901 1–211901 3
6. Taylor GI (1934) Proc R Soc A 145:362
7. Orowan E (1934) Zeit Phys 89:605
8. Polanyi M (1934) Zeit Phys 89:660
9. Whang Y, Chen M, Zhou F, Ma E (2002) Nature 419:912
10. Saito T, Furuta T, Hwang JH, Kuramoto S, Nishino K, Suzuki N, Chen R, Yamada A, Ito K, Seno Y, Nonaka T, Ikehata H, Nagasako N, Iwamoto C, Ikuhara Y, Sakuma T (2003) Science 300:464
11. Wetscher F, Vorhauer A, Stock R, Pippan R (2004) Mater Sci Eng A 387–389:809
12. Esrtrin Y, Molitnikov A, Davies CHJ, Lapovok R (2008) J Mech Phys Solids 56:1186
13. Furuta T, Kuramoto S, Ohsuna T, Horita Z (2010) In: Proceedings of the 2nd international symposium on steel science (ISSS 2009), 21–24 October 2009, The Iron and Steel Institute of Japan, ISSS, Kyoto, Japan (in press)
14. Morito S, Tanaka H, Konishi R, Furuhara T, Maki T (2003) Acta Mater 51:1789
15. Zhilyaev AP, Langdon TG (2008) Prog Mater Sci 53:893
16. Tsuji N, Maki T (2009) Scr Mater 60:1044
17. Zhao YH, Liao XZ, Horita Z, Langdon TG, Zhu YT (2008) Mater Sci Eng A493:123
18. Furuta T, Hara M, Horita Z, Kuramoto S (2009) Int J Mater Res 100:1211
19. Ivanisenko Yu, MacLaren I, Sauvage X, Valiev RZ, Frecht HJ (2006) Acta Mater 54:1659
20. Li JG, Umemoto M, Todaka Y, Fujisaku K, Tuchiya K (2008) Rev Adv Mater Sci 18:577

21. Takaki S, Kawasaki K, Kimura Y (2001) J Mater Process Technol 1:359
22. Krenn C, Roundy D, Morris JW, Cohen M (2001) Mater Sci Eng A319–321:111
23. Landolt-Börnstein 29 29-30 Springer-Verlag, Berlin Heidelberg New York London Paris Tokyo Hong Kong Barcelona Budapest
24. Hara M, Furuta T, Kuramoto S, Shimizu Y, Yano T, Takesue N (2009) Int J Mater Res 100:345
25. Kuramoto S, Furuta T, Nagasako N, Hara M (2010) Mater Sci Forum 638–642:3858
26. Withey E, Ye J, Minor A, Kuramoto S, Chrzan DC, Morris JW (2009) Exp Mech 50:37